Two-Color Grating Magneto-Optical Trap for Narrow-Line Laser Cooling

S. Bondza[1,2,*] C. Lisdat[1,†] S. Kroker[1,3,4] and T. Leopold[1,2]

[1]*Physikalisch-Technische Bundesanstalt, Bundesallee 100, Braunschweig 38116, Germany*

[2]*Deutsches Zentrum für Luft- und Raumfahrt e.V. (DLR), Institut für Satellitengeodäsie und Inertialsensorik, c/o Leibniz Universität Hannover, Callinstraße 36, Hannover 30167, Germany*

[3]*Technische Universität Braunschweig, Institut für Halbleitertechnik, Hans-Sommer-Str. 66, Braunschweig 38106, Germany*

[4]*LENA Laboratory for Emerging Nanometrology, Langer Kamp 6, Braunschweig 38106, Germany*

We demonstrate the two-color cooling and trapping of alkaline-earth atoms in a grating magneto-optical trap (GMOT). The trap is formed by a single incident laser beam together with four secondary beams that are generated via diffraction from a nanostructured wafer. A grating structure for a GMOT operating with strontium atoms is optimized and fabricated. We trap 10^6 ^{88}Sr atoms on the $^1S_0 \rightarrow \, ^1P_1$ transition at 461 nm and transfer 25% of these atoms to the second cooling stage on the narrower $^1S_0 \rightarrow \, ^3P_1$ intercombination transition at 689 nm, preparing a sample of 2.5×10^5 atoms at 5 μK. These results demonstrate the applicability of the GMOT technology in conjunction with two widely differing wavelengths and enable the continued miniaturization of alkaline-earth-based quantum technologies like optical atomic clocks.

I. INTRODUCTION

Laser-cooled and trapped atoms provide a successful technological basis for second-generation quantum sensors. Among these devices are highly sensitive magnetometers [1,2], gravimeters [3–5], quantum computers [6,7], and optical atomic clocks [8]. All these devices experience a transition from a laboratory to field-based environment [9–12] and a beginning commercialization [13], which requires a high degree of miniaturization and integration of the basic enabling technologies.

Compact and scalable devices for cooling and trapping of atoms at a single wavelength have recently been demonstrated in the form of grating magneto-optical traps (GMOTs) [14–18], where one incident laser beam produces secondary beams via diffraction on a set of gratings. Combined, these beams lead to cooling and confinement of the atoms above the gratings when used in conjunction with a suitable magnetic quadrupole field. Advanced atom interferometers, as well as optical atomic

clocks based on cold atoms benefit from an ultranarrow electronic transition [8,19], which is provided for example in alkaline-earth-like atoms. However, due to the broad linewidth of the $^1S_0 \rightarrow \, ^1P_1$ transition in alkaline-earth atoms and the correspondingly high Doppler temperature, additional cooling on the narrower $^1S_0 \rightarrow \, ^3P_1$ transition is commonly applied to reach temperatures in the low μK range. The wavelength ratio of these two transitions is typically about 1.5, which leads to significant deviations of the respective diffraction properties on a grating. The difference in diffraction angle leads to a spatial shift of the trapping volumes complicating transfer from the first to the second cooling stage. Furthermore, in a GMOT design it is generally desirable to have a low zeroth-order diffraction efficiency for the incident light, which is often achieved by choosing a grating height that corresponds to a quarter of the incident wavelength [17,20,21] and cannot be fulfilled for both wavelengths simultaneously. Additionally, the optimum diffraction efficiency in first order is fixed by the number of grating segments and should be identical for TE and TM polarization components. It is easy to see that the limited number of parameters in grating design do not allow an optimization of the full set of diffraction properties, especially for widely varying wavelengths.

In this paper we present a grating structure dedicated to magneto-optical trapping of alkaline-earth atoms in a GMOT and demonstrate the first two-stage cooling of ^{88}Sr atoms in such a system. We enhance the optimization

---

*saskia.bondza@ptb.de

†christian.lisdat@ptb.de

parameter space by applying a thin gold coating on top of the grating, which allows us to balance the diffraction efficiencies for 461 and 689 nm. A central hole in the wafer removes the relevance of the zeroth-order diffraction efficiency for the second cooling stage at 689 nm, as the atoms have coalesced to a cloud of millimeter size at the end of the first cooling stage.

With a grating chip fabricated according to our design, we prepare 2.5×10^5 atoms at a temperature of 5 μK, which is sufficiently low for a transfer into a typical optical lattice as used in atomic clocks [22,23]. We describe the transfer process from the first to the second cooling stage with an achieved transfer efficiency of 25%.

II. GRATING DESIGN

The idea of restoring forces in a magneto-optical trap (MOT) is most easily realized by laser beams incident along the x, y, and z axis of the quadrupole field $\mathbf{B} = b\{x, y, -2z\}$ with circular polarization. Choosing the correct handedness the σ transitions are predominantly driven, which leads to a restoring force. In a GMOT this is not the case, as the secondary beams form an oblique angle with all principal axes. Hence, coupling of the secondary beams to all (σ^+, π, σ^-) transitions must be evaluated [24,25]. Looking at the laser-induced acceleration of an atom at rest along the symmetry axis z of the quadrupole field, we see that the acceleration from the secondary beams exhibits a trapping and an antitrapping contribution due to coupling to all $\Delta m = 0, \pm 1$ transitions as illustrated in Fig. 1 [24]. Nevertheless, the figure shows that stable trapping is possible as the combined acceleration of incident and secondary beams can lead to an overall restoring force, depending on the choice of grating parameters.

Here, we present our design of a grating structure for two-stage cooling of strontium atoms. The first stage utilizes the $^1S_0 \rightarrow ^1P_1$ transition with a linewidth of 30.2 MHz at a wavelength of 461 nm [26] and the second stage the $^1S_0 \rightarrow ^3P_1$ transition with a linewidth of 7.5 kHz at a wavelength of 689 nm [27]. The second stage is subdivided into a broadband (BB) phase, where the laser linewidth is artificially broadened to the megahertz range, and a single-frequency (SF) phase, where the laser operates with a linewidth on the order of the transition linewidth. This procedure increases the transfer efficiency of atoms from the first stage to the second cooling stage [28]. When designing a grating for two very different wavelengths one should keep in mind several considerations that are connected to the wavelength dispersion of the diffraction angle and diffraction efficiency:

(I) Differences in diffraction angle result in an unfavorable axial shift and therefore only partial overlap of trapping volumes. The trapping volume for each wavelength is defined as the volume in space where light from both the primary and all secondary beams of the respective color is present, see Fig. 2. A small overlap of both volumes complicates transfer of the atoms from the first- to the second-stage MOT.

(II) A diffraction efficiency of $1/N$ for both colors, where N is the number of secondary beams, leads to intensity balance [14], characterized by a vanishing net force in the absence of a magnetic field, i.e., the intensity-weighted k vectors of all beams adding to zero. Additionally, for both trapping wavelengths equal diffraction efficiencies of the TE and TM polarization mode are useful in order to conserve the incident circular polarization, as radial trapping weakens otherwise. TE polarization corresponds to p polarization with the oscillation direction of the electric field parallel to the grating grooves and TM polarization corresponds to s polarization with the oscillation direction of the electric field perpendicular to the grating grooves. Both waves must have equal amplitudes and a phase shift of $\pi/2$ to yield circular polarization.

(III) The zeroth-order diffraction for both wavelengths should be minimized, as it contributes predominantly to an antitrapping acceleration of the atoms [21].

(IV) Varying the grating period shows three effects. First of all, the overlap of the trapping volumes increases for larger grating periods. Secondly, larger diffraction angles are obtained for shorter grating periods resulting in increased radial and axial restoring forces. At last, a geometry for simultaneous optimization of first-order diffraction efficiencies to about $1/N$ for both wavelengths and polarization modes cannot be found for all grating periods.

(V) Intensity balance is of particular relevance for magneto-optical trapping on broad transitions, when the maximum achievable magnetic field gradient is not sufficient to enable spatially well-resolved addressing of the transitions. The effect of deviations from optimum diffraction efficiency are shown in Fig. 1(b). Here, deviations from intensity balance, characterized by the figure of merit η, which is the ratio of the diffraction efficiency to its ideal value of $1/N$, result in a shift of the equilibrium position in the trap with respect to the magnetic field minimum and a reduced trap depth. In contrast, axial cooling on the narrow transition can actually benefit from intensity imbalance when cooling with laser intensities I well above saturation ($s = I/I_{\text{sat}} \gg 1$). As shown in Fig. 1(c), the trap depth increases for $\eta < 1$ due to a decrease of the antitrapping contribution of the secondary beams relative to the trapping contribution of the incident beam. The trapping contribution of the secondary beams is not significantly reduced due to saturation.

With these constraints in mind, we design a grating structure, which is optimized for two-stage magneto-optical trapping of strontium atoms. The zeroth-order diffraction is geometrically minimized for 461 nm, while
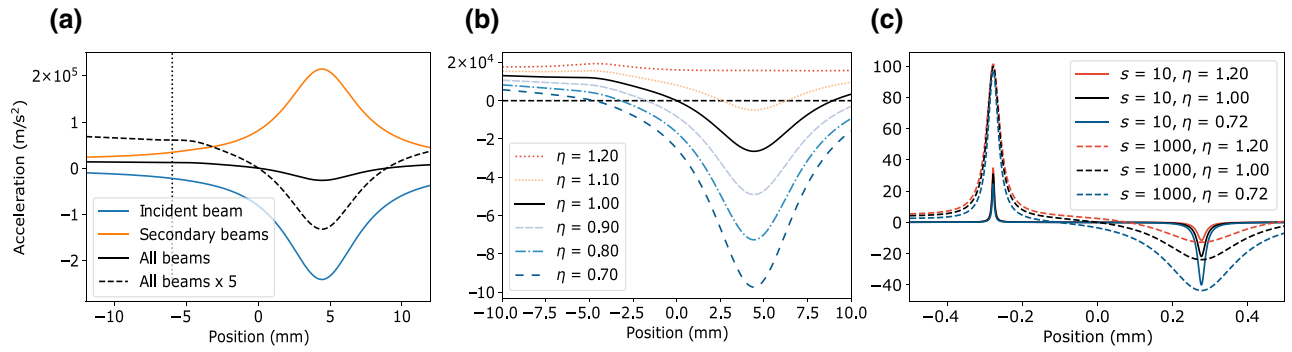
FIG. 1.   Illustration of axial acceleration acting on an atom at rest along the symmetry axis z of the quadrupole field for both cooling stages. The magnetic field minimum marks zero on the z axis. (a) Contribution of incident and secondary beams to the axial acceleration in the first-stage MOT with a saturation parameter $s = 0.5$, a detuning of -32 MHz, magnetic field gradient $dB/dz = 5$ mT/cm, and diffraction angle $\alpha_{461} = 31°$. The dotted vertical line marks the position of the grating. (b) Influence of intensity imbalance, characterized by η, on the total axial acceleration in the first-stage MOT. Imbalance ($\eta \neq 1$) leads to a shift of the steady-state position, as seen by the intersection of the acceleration curve with the zero acceleration line (dashed black line). (c) Total axial acceleration for different saturation parameters and levels of intensity balance in the second-stage MOT. The case $\eta = 0.72$ corresponds to the manufactured grating, see Table I. $\Delta = -400$ kHz, $dB/dz = 0.9$ mT/cm, and $\alpha_{689} = 50°$.

for 689 nm a 3-mm hole in the center of the chip suppresses back reflection in the relevant volume for second-stage trapping. The parameters for optimization are grating period, height, fill factor, and the thickness of an additional gold layer. Varying the fill factor for a fixed grating period and height allows the ratio of TE to TM diffraction efficiency to be changed [16,21]. The gold layer is introduced to reduce the diffraction efficiency for 461 nm relative to 689 nm by means of the higher absorption of gold in the blue spectrum.
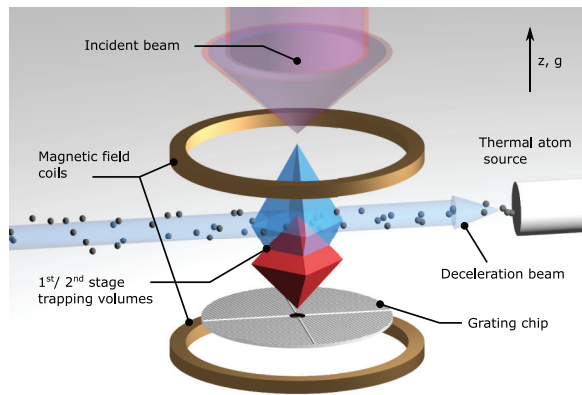

FIG. 2.   Schematic representation of the experimental setup. The 461-nm and 689-nm laser beams with 18-mm diameter are incident on the grating chip, producing secondary beams by diffraction. The volumes where light from the incident and each secondary beam overlap form an octahedron above the chip, where the elongation is determined by the diffraction angle. Magnetic field coils are mounted symmetrically to a point in the overlap of the trapping volumes. Radially incident atoms from a thermal source are slowed by a counterpropagating deceleration beam.

One can then devise a cost function that contains the relative deviations of all diffraction efficiencies from their target value and weigh the individual contributions by priority. Optimized grating parameters are found by evaluating the cost function with a simulation program for different parameter sets. We use rigorous coupled wave analysis (RCWA) [29] to scan grating height and duty cycle for various grating periods and thicknesses of the gold layer for both silver and aluminium substrates. A four-segment design sets the targeted first-order diffraction efficiency to 25% and enables lower cost functions compared to a three-segment design. Best results are obtained for an 900-nm period aluminium grating corresponding to diffraction angles of $\alpha_{461} = 31°$ and $\alpha_{689} = 50°$ for 461 and 689 nm, respectively. The sensitivity of the targeted diffraction efficiencies on the separate grating parameters is given by the simulated gradients at the design value. The optimum height of the grating grooves is evaluated to 109 nm with gradients of the first-order diffraction efficiency at 461 and 689 nm of 0.3 %/nm (0.1 %/nm) and 0.6 %/nm (0.2 %/nm) for TE (TM) polarization,

TABLE I.   Diffraction efficiencies (averaged over TE and TM modes) of the grating in percent as designed and as measured for 461 and 689 nm. The measured intensity imbalance factor η equals unity and 0.72 for first and second cooling stage, respectively.

	Zeroth order		First order	
	Simulated	Measured	Simulated	Measured
461 nm	8.4	7(1)	26.6	25(1)
689 nm	46.6	50(2)	21.4	18(1)

respectively. Further, we find a fill factor of 0.283 corresponding to a groove width of 645.3 nm with gradients of the first-order diffraction efficiency at 461 and 689 nm of 0.07 %/nm (0.02 %/nm) and 0.03 %/nm (0.2 %/nm) for TE (TM) polarization, respectively, to be optimal.

The grating is manufactured in the Physikalisch-Technische Bundesanstalt clean-room facilities. A silicon wafer is coated with a base layer of 100-nm aluminum. The grating lines are produced using electron-beam lithography and a lift-off process. The gold layer is evaporated on top of the structure. Due to the nature of the manufacturing process an 8-nm-thick oxide layer forms between the aluminum grating and the gold coating layer reducing the first-order diffraction efficiency by 3% and 2% for 461 and 689 nm, respectively. The oxide layer is identified through scatterometry. We compensate this deviation from the designed layout by adjusting the thickness of the gold layer from 20 to 10 nm in a second-generation grating, which we use for the investigations in this paper. For the gold-coating layer thickness, the gradients of the first-order diffraction efficiency at 461 and 689 nm are -0.3 %/nm (-0.8 %/nm) and 0.3 %/nm (0.1 %/nm) for TE (TM) polarization, respectively.

The diffraction efficiencies of this grating are measured experimentally and are in general agreement with simulated values as presented in Table I. The ratio of the first-order diffraction efficiency for TE and TM polarization mode is ≥ 0.89 at both wavelengths. The grating geometry is inspected with atomic force microscopy, scatterometry, and scanning electron microscopy. Good agreement between design and fabricated geometry suggests that deviations between measurement and simulation are most likely explained by uncertainties in the material dispersion properties of the thin-film layers and measurement uncertainties on the gold and oxide layer thicknesses.

In the second-stage MOT, the maximum optical acceleration is only 10 times stronger than gravity such that the effect of the latter can no longer be neglected, see Fig. 1(c). The SF MOT forms at a height where gravity is balanced by optical acceleration so that trapped atoms will gather on the flank of the acceleration peak opposing gravity. In a microgravity environment the atoms will scatter on both acceleration peaks.

In the direction opposing the incident beam, the acceleration results from the difference of a large trapping and a slightly smaller antitrapping light force, analog to the first cooling stage, see Fig. 1(a). Choosing the equilibrium position on that scattering peak thus leads to an overall increase in scattering events and, hence, a higher temperature in the MOT is expected compared to the gravitationally inverted situation or a six-beam MOT. In this work, we operate in the above described "worst case" geometry, with gravity pointing away from the chip surface to prove the general feasibility of second-stage cooling of strontium in a GMOT, independent of orientation.

III. RESULTS

The grating chip is mounted inside an ultrahigh vacuum system comprised of a standard spherical octagon. Two vacuum pumps, an 80 l/S nonevaporable getter (NEG) pump and a 40 l/S ion pump are mounted on opposite sides of the vacuum system to have a versatile test chamber for fast probe exchange. For the generation of a quadrupole field with variable magnetic field gradients up to 6 mT/cm, two wire coils are mounted within the vacuum system. Their symmetry plane lies 6 mm above the grating surface. Additional coils outside the vacuum system allow fine positioning of the magnetic field minimum. Atoms are evaporated from a thermal source following Ref. [30]. In contrast to most other experiments trapping strontium atoms, we do not employ a Zeeman slower between the thermal source and our MOT. Atoms are decelerated by a slowing beam, red detuned by 220 MHz with respect to the $^1S_0 \rightarrow {}^1P_1$ transition, 3-mm beam diameter and a laser power of 20 mW as depicted in Fig. 2. The lower fraction of slow atoms compared to a Zeeman-slowed beam is partially compensated by a short distance between the atom source and the trapping region of only 14 cm. With the deceleration beam turned off, the MOT loading rate is reduced by a factor of >100.

The base vacuum pressure in our system is 2×10^{-10} mbar and rises up to 5×10^{-9} mbar for temperatures of the strontium oven up to 390 °C.

A beam-shaping unit consisting of a variable magnification telescope and a flat-top beam shaper combines fiber-coupled light at 461 and 689 nm, producing an 18-mm diameter bichromatic laser beam with circular polarization and a flat-top intensity profile. The beam profile can be adjusted by varying the diameter of the input beam of the flat-top beam shaper with the variable magnification telescope. We fine adjust the beam profile in this way to yield the maximum number of atoms. However, in other works (truncated) Gaussian beams were also used successfully for GMOT operation [14,17,18]. The grating structure is illuminated with maximum laser power of 53 mW corresponding to an intensity of $I \approx 0.5 I_{\text{sat}}$ at 461 nm and 15 mW corresponding to an intensity of $I \approx 2000 I_{\text{sat}}$ at 689 nm, respectively.

The $^1S_0 \rightarrow {}^1P_1$ transition is not closed due to decay from the $^1P_1$ state to the $^1D_2$ state and subsequent decay to the $^3P_2$ state. To close this loss channel we employ a standard repump scheme outlined in Ref. [31] using two additional lasers with wavelengths of 679 and 707 nm. Both wavelengths are combined using a dichroic mirror and illuminate the atoms radially. Another radial axis is used for a laser beam resonant with the $^1S_0 \rightarrow {}^1P_1$ transition at 461 nm for fluorescence detection.

The light sources for 461, 679, and 707 nm are commercial external cavity diode lasers, which are stabilized to a wave meter. Narrow-linewidth laser light at 689 nm

is produced with a home-built laser system based on self-injection locking [32] of a single-frequency laser diode (Eblana Photonics). Long-term frequency stability is achieved by referencing the laser to a vacuum-housed optical resonator. We estimate a short-term laser linewidth of 50 kHz from the in-loop error signal of the feedback loop to the resonator. A high-power Fabry-Pérot laser diode is injection locked from this laser system, yielding up to 15 mW of light incident on the grating.

The fluorescence light scattered by the atoms from the detection beam is imaged parallelly to the grating surface onto either a camera or photomultiplier tube with a magnification of 0.8.

The experimental sequence to cool atoms to 5 μK in the SF MOT is depicted in Fig. 3. It starts with loading about 10^6 atoms into the first cooling stage. This is done by shining in the 18-mm diameter red-detuned first-stage cooling beam onto the grating and the deceleration beam onto the atom source. The diameter of the cooling beam results in a maximum radial extension of the first-stage trapping volume at a height of 7.5 mm above the chip surface, 1.5 mm above the symmetry point of the *in vacuo* magnetic field coils. A quadrupole magnetic field with a gradient of 5 mT/cm along the z axis is produced with the wire coils. An external offset magnetic field is applied along the z direction, to move the magnetic field zero of the quadrupole field towards the symmetry point of the trapping volume. After loading atoms for 300 ms the deceleration beam is turned off, removing the additional radiation pressure and changing the MOT position slightly. The second-stage cooling laser is turned on at full power, with a laser linewidth broadened to 1.6 MHz by frequency modulation at 50 kHz. The external magnetic offset field and the first-stage cooling laser power are ramped to zero. This moves the atoms towards the grating chip, inside the second-stage trapping volume, see Fig. 2. After moving the atoms, the magnetic field gradient is switched to 0.3 mT/cm to reduce the Zeeman shift to within the laser bandwidth. After cooling for 15 ms the BB MOT is spatially compressed by linearly increasing the magnetic field gradient up to 1 mT/cm. At the same time, the laser intensity is reduced to reach lower temperatures.

The SF MOT phase starts by turning off the artificial laser linewidth broadening and increasing the laser intensity to the maximum value of $s = 2000$. Over the course of several 10 ms, the intensity is reduced. In the fluorescence images in Fig. 3, a further compression of the atoms in the SF phase compared to the BB phase is visible. We are able to trap 10^6 atoms in the first cooling stage and achieve a transfer efficiency of 25% to the SF MOT, corresponding to 2.5×10^5 atoms.

We measure the lifetime in the first cooling stage as a function of magnetic field gradient and laser intensity. Lifetime measurements are performed by loading the MOT, turning off the deceleration beam, which effectively
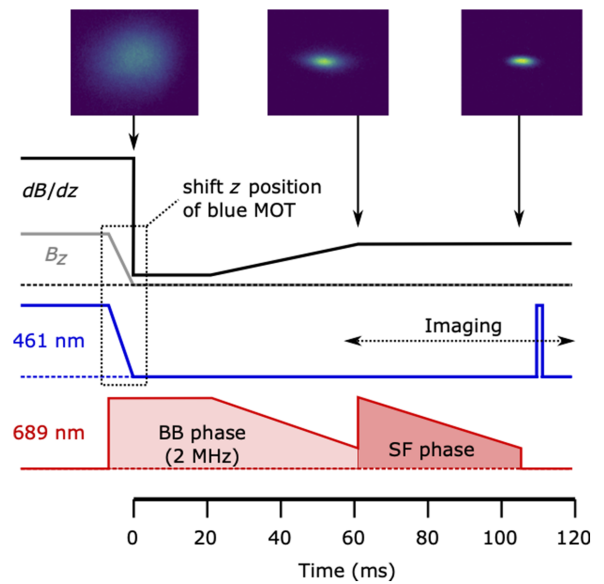

FIG. 3. Time evolution of experimental parameters: Axial magnetic field gradient (black), axial magnetic offset field (gray), 461-nm laser intensity (blue) and 689-nm laser intensity (red). Fluorescence images of the MOT at different times during the cooling sequence are shown. For details see information in the text.

stops loading atoms, and measuring the relative number of atoms after a variable wait time before detection.

We find the lifetime to increase with magnetic field gradient and laser intensity as depicted in Fig. 4, similar as in Ref. [18]. We measure a lifetime of up to 700 ms with our maximum available laser intensity and magnetic field gradient at a pressure of 3×10^{-9} mbar, which is close to being vacuum limited [33]. The vacuum pressure is limited by outgassing from the strontium oven, which is commonly handled by differential pumping. The necessity for a relatively high laser intensity can be traced back to the reduced trap depth in the GMOT configuration. From Fig. 1(a) one can infer that the total axial acceleration, and hence trap depth, for a given laser intensity is about 10 times smaller than in a conventional six-beam MOT, where the magnitude of restoring acceleration is roughly the size of the contribution from the incident beam. An increase in trap depth with magnetic field gradient is expected as long as the Zeeman shift remains smaller than the laser detuning within the trapping volume [34].

We characterize the MOT temperature via the time-of-flight expansion method using fluorescence imaging with 100-μS stroboscopic illumination from the detection beam. The size of the atom cloud σ is then plotted as a function of time t and fitted according to $\sigma^2(t) = \sigma_0^2 + (k_B T/M) \times t^2$, where σ_0 is the initial size of the atom cloud, k_B denotes Boltzmann's constant, M the atomic mass, and T the atomic temperature. We fit separate temperatures for the axial and radial projection of the MOT
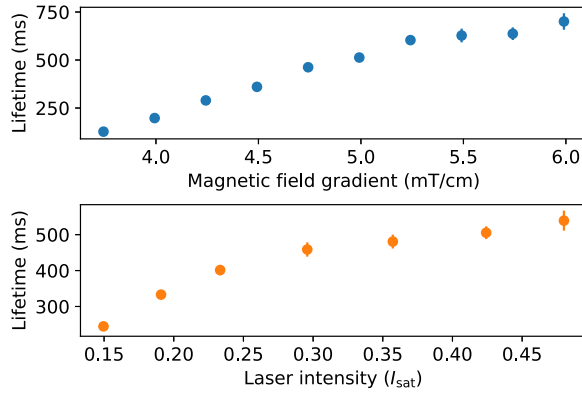
FIG. 4. Lifetime in the first-stage MOT in dependence of laser intensity with $dB/dz = 5$ mT/cm and magnetic field gradient with $I = 0.48I_{sat}$. Error bars are about the size of the data points.

FIG. 5. Temperature in the BB and SF MOT in radial and axial direction as a function of laser intensity.

onto the camera. We find the temperature in the first-stage MOT to increase with increasing intensity of the laser beams as is generally expected [35]. At $s = 0.5$ we measure an axial temperature of 3.5–4 mK and a radial temperature of 7.5–8 mK. Lowering the intensity at the end of the cooling cycle, we reach temperatures of 1.2 and 4.5 mK in axial and radial direction, respectively. In a conventional six-beam configuration temperatures of 1 mK can be achieved with these parameters [35]. Higher temperatures can qualitatively be explained by the antitrapping contribution from the secondary beams.

We measure the temperature in the second-stage BB and SF MOT as a function of the incident laser intensity. In the BB MOT, temperatures of around 10 μK are reached as seen in Fig. 5, which is comparable to the standard six-beam configuration [23]. In the SF MOT we reach minimum temperatures of slightly below 5 μK both in radial and axial direction. We find the temperature to decrease with laser intensity, as expected, until it reaches a minimum at around $20I_{sat}$–$30I_{sat}$. For lower laser intensities the MOT temperature increases again. In a six-beam geometry temperature in the SF MOT decreases continuously with intensity down to sub-μK [36]. We suspect that the temperature is limited by the antitrapping interaction with the secondary beams, as discussed earlier, and expect that lower temperatures can be reached by mounting the grating such that the secondary beams counteract gravity, which suppresses interaction with the primary beam and thus reduces the scattering rate in the SF MOT.

IV. DISCUSSION

We demonstrate magneto-optical trapping of alkaline-earth atoms in a GMOT on both the $^1S_0 \rightarrow ^1P_1$ and the narrow-line $^1S_0 \rightarrow ^3P_1$ cooling transition. The sequential magneto-optical trapping on two transitions with different wavelengths is shown in a GMOT. We prepare 2.5×10^5 ^{88}Sr atoms at a temperature of 5 μK, which is
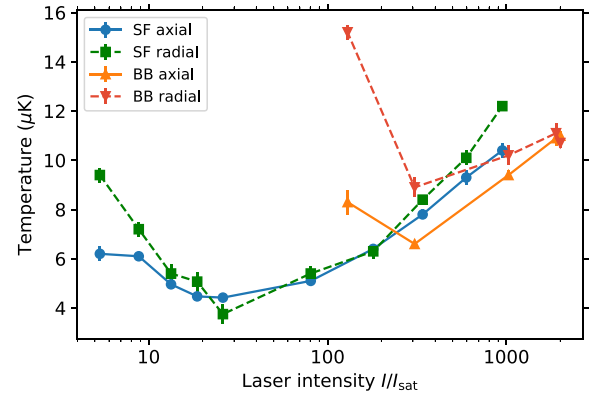
sufficiently cold for loading into an optical lattice used in optical clocks, with typical trap depths on the order of 10 μK. We give general guidelines for the design of a grating for two-color magneto-optical trapping and expect that the results of our work can be transferred to other atomic species that require sequential cooling stages, such as ytterbium.

We expect that the number of trapped atoms can be increased significantly by a higher flux of slow atoms using a Zeeman slower. Differential pumping between the atom source and science chamber would improve the vacuum level and reduce the loss rate from the MOT. Additionally, higher loading rates can be achieved in a GMOT by loading atoms along the axial direction of the grating [17]. To improve our understanding of the single-beam geometry we plan an in-depth study based on Monte Carlo simulations for cooling on narrow linewidth transitions investigating the higher temperatures we observe and compare this to the standard six-beam case. Additionally, we plan simulations regarding trap depths and lifetime aiming to identify possible loss channels.

Our results prove that the GMOT technology is compatible with multicolor magneto-optical trapping. This enables highly compact quantum sensors based on alkaline-earth-like atoms, e.g., optical atomic clocks and atom interferometers.

---

[1] S. Wildermuth, S. Hofferberth, I. Lesanovsky, E. Haller, L. M. Andersson, S. Groth, I. Bar-Joseph, P. Krüger, and J. Schmiedmayer, Microscopic magnetic-field imaging, Nature **435,** 440 (2005).

[2] Y. Cohen, K. Jadeja, S. Sula, M. Venturelli, C. Deans, L. Marmugi, and F. Renzoni, A cold atom radio-frequency magnetometer, Appl. Phys. Lett. **114,** 073505 (2019).

[3] M. Kasevich and S. Chu, Measurement of the gravitational acceleration of an atom with a light-pulse atom interferometer, Appl. Phys. B **54,** 321 (1992).

[4] J. E. Debs, P. A. Altin, T. H. Barter, D. Döring, G. R. Dennis, G. McDonald, R. P. Anderson, J. D. Close, and N. P. Robins, Cold-atom gravimetry with a Bose-Einstein condensate, Phys. Rev. A **84,** 033610 (2011).

[5] S. Abend, M. Gebbe, M. Gersemann, H. Ahlers, H. Müntinga, E. Giese, N. Gaaloul, C. Schubert, C. Lämmerzahl, W. Ertmer, W. P. Schleich, and E. M. Rasel, Atom-Chip Fountain Gravimeter, Phys. Rev. Lett. **117,** 203003 (2016).

[6] M. Saffman, Quantum computing withatomic qubits and Rydberg interactions: Progress and challenges, J. Phys. B: At., Mol., Opt. Phys. **49,** 202001 (2016).

[7] L. Henriet, L. Beguin, A. Signoles, T. Lahaye, A. Browaeys, G.-O. Reymond, and C. Jurczak, Quantum computing with neutral atoms, Quantum **4,** 327 (2020).

[8] A. D. Ludlow, M. M. Boyd, J. Ye, E. Peik, and P. O. Schmidt, Optical atomic clocks, Rev. Mod. Phys. **87,** 637 (2015).

[9] J. Grotti *et al.* Geodesy and metrology with a transportable optical clock, Nat. Phys. **14,** 437 (2018).

[10] N. Ohmae, M. Takamoto, Y. Takahashi, M. Kokubun, K. Araki, A. Hinton, I. Ushijima, T. Muramatsu, T. Furumiya, Y. Sakai, N. Moriya, N. Kamiya, K. Fujii, R. Muramatsu, T. Shiimado, and H. Katori, Transportable strontium optical lattice clocks operated outside laboratoryat the level of 10^{-18} uncertainty, Adv. Quantum Technol. **4,** 2100015 (2021).

[11] B. Fang, I. Dutta, P. Gillot, D. Savoie, J. Lautier, B. Cheng, C. L. G. Alzar, R. Geiger, S. Merlet, F. P. D. Santos, and A. Landragin, Metrology with atom interferometry: Inertial sensors from laboratory to field applications, J. Phys.: Conf. Ser. **723,** 012049 (2016).

[12] M. Lin, H. Denker, and J. Müller, A comparison of fixed- and free-positioned pointmass methods for regional gravity field modeling, J. Geodyn. **125,** 32 (2019).

[13] V. Menoret, P. Vermeulen, N. L. Moigne, S. Bonvalot, P. Bouyer, A. Landragin, and B. Desruelle, Gravity measurements below 10^{-9} g with a transportable absolute quantum gravimeter, Sci. Rep. **8,** 104207 (2018).

[14] M. Vangeleyn, P. F. Griffin, E. Riis, and A. S. Arnold, Laser cooling with a single laser beam and a planar diffractor, Opt. Lett. **35,** 3453 (2010).

[15] C. C. Nshii, M. Vangeleyn, J. P. Cotter, P. F. Griffin, E. A. Hinds, C. N. Ironside, P. See, A. G. Sinclair, E. Riis, and A. S. Arnold, A surface-patterned chip as a strong source of ultracold atoms for quantum technologies, Nat. Nanotechnol. **8,** 321 (2013).

[16] J. P. McGilligan, P. F. Griffin, R. Elvin, S. J. Ingleby, E. Riis, and A. S. Arnold, Grating chips for quantum technologies, Sci. Rep. **7,** 384 (2017).

[17] D. S. Barker, E. B. Norrgard, N. N. Klimov, J. A. Fedchak, J. Scherschligt, and S. Eckel, Single-Beam Zeeman Slower and Magneto-Optical Trap Using a Nanofabricated Grating, Phys. Rev. Appl. **11,** 064023 (2019).

[18] A. Sitaram, P. K. Elgee, G. K. Campbell, N. N. Klimov, S. Eckel, and D. S. Barker, Confinement of an alkaline-earth element in a grating magneto-optical trap, Rev. Sci. Instrum. **91,** 103202 (2020).

[19] L. Hu, N. Poli, L. Salvi, and G. M. Tino, Atom Interferometry with the Sr Optical Clock Transition, Phys. Rev. Lett. **119,** 263601 (2017).

[20] J. P. McGilligan, P. F. Griffin, E. Riis, and A. S. Arnold, Diffraction-grating characterization for cold-atom experiments, J. Opt. Soc. Am. B **33,** 1271 (2016).

[21] J. P. Cotter, J. P. McGilligan, P. F. Griffin, I. M. Rabey, K. Docherty, E. Riis, A. S. Arnold, and E. A. Hinds, Design and fabrication of diffractive atom chips for laser cooling and trapping, Appl. Phys. B **122,** 172 (2016).

[22] S. Falke, N. Lemke, C. Grebing, B. Lipphardt, S. Weyers, V. Gerginov, N. Huntemann, C. Hagemann, A. Al-Masoudi, S. Häfner, S. Vogt, U. Sterr, and C. Lisdat, A strontium lattice clock with 3×10^{-17} inaccuracy and its frequency, New J. Phys. **16,** 073023 (2014).

[23] N. Poli, M. Schioppo, S. Vogt, S. Falke, U. Sterr, C. Lisdat, and G. M. Tino, A transportable strontium optical lattice clock, Appl. Phys. B **117,** 1107 (2014).

[24] M. Vangeleyn, Ph.D. thesis, 2011.

[25] M. Vangeleyn, P. F. Griffin, E. Riis, and A. S. Arnold, Single-laser, one beam, tetrahedral magneto-optical trap, Opt. Express **17,** 13601 (2009).

[26] T. L. Nicholson, S. L. Campbell, R. B. Hutson, G. E. Marti, B. J. Bloom, R. L. McNally, W. Zhang, M. D. Barrett, M. S. Safronova, G. F. Strouse, W. L. Tew, and J. Ye, Systematic evaluation of anatomic clock at 2×10^{-18} total uncertainty, Nat. Commun. **6,** 6896 (2015).

[27] M. Yasuda, T. Kishimoto, M. Takamoto, and H. Katori, Photoassociation spectroscopy of ^{88}Sr: Reconstruction of the wave function near the last node, Phys. Rev. A **73,** 011403(R) (2006).

[28] H. Katori, T. Ido, Y. Isoya, and M. Kuwata-Gonokami, Magneto-Optical Trapping and Cooling of Strontiumatoms Down to the Photon Recoil Temperature, Phys. Rev. Lett. **82,** 1116 (1999).

[29] M. G. Moharam and T. K. Gaylord, Rigorous coupled-wave analysis of grating diffraction—*E*-mode polarization and losses, J. Opt. Soc. Am. **73,** 451 (1983).

[30] M. Schioppo, N. Poli, M. Prevedelli, S. Falke, C. Lisdat, U. Sterr, and G. M. Tino, A compact and efficient strontium oven for laser-cooling experiments, Rev. Sci. Instrum. **83,** 103101 (2012).

[31] S. Falke, H. Schnatz, J. S. R. Vellore Winfred, T. Middelmann, S. Vogt, S. Weyers, B. Lipphardt,

G. Grosche, F. Riehle, U. Sterr, and C. Lisdat, The ^{87}Sr optical frequency standard at PTB, Metrologia **48**, 399 (2011).

[32] Q. Lin, M. A. V. Camp, H. Zhang, B. Jelenković, and V. Vuletić, Long-external-cavity distributed Bragg reflector laser with subkilohertz intrinsic linewidth, Opt. Lett. **37**, 1989 (2012).

[33] S. B. Nagel, C. E. Simien, S. Laha, P. Gupta, V. S. Ashoka, and T. C. Killian, Magnetic trapping of metastable $^3P_2$ atomic strontium, Phys. Rev. A **67**, 011401 (2003).

[34] S. Yoon, Y. Choi, S. Park, W. Ji, J.-H. Lee, and K. An, Characteristics of single-atom trapping in a magneto-optical trap with a high magnetic-field gradient, J. Phys.: Conf. Ser. **80**, 012046 (2007).

[35] X. Xu, T. H. Loftus, J. L. Hall, A. Gallagher, and J. Ye, Cooling and trapping of atomic strontium, J. Opt. Soc. Am. B **20**, 968 (2003).

[36] T. H. Loftus, T. Ido, M. M. Boyd, A. D. Ludlow, and J. Ye, Narrow line cooling and momentum-space crystals, Phys. Rev. A **70**, 063413 (2004).

Correction: The previously published Figure 2 was missing all labels and has been replaced.